

# A Second-Order, Variable-Resolution, Weakly-Compressible Smoothed Particle Hydrodynamics Scheme

Abhinav Muta<sup>a,1</sup>, Pawan Negi<sup>a,b,1,\*</sup>, Prabhu Ramachandran<sup>a</sup>

<sup>a</sup>*Department of Aerospace Engineering, Indian Institute of Technology Bombay, Powai,  
Mumbai 400076*

<sup>b</sup>*Department of Applied Mathematics, Illinois Institute of Technology, Chicago, 60616*

---

## Abstract

The smoothed particle hydrodynamics (SPH) method has been widely used to simulate incompressible and slightly compressible fluid flows. Adaptive refinement strategies to dynamically increase the resolution of the particles to capture sharp gradients in the flow have also been developed. However, most of the SPH schemes in the literature are not second-order convergent (SOC). Both second-order convergence and adaptive resolution are considered grand challenge problems in the SPH community. In this paper, we propose, for the first time, a second-order convergent (SOC) adaptive refinement strategy along with a SOC weakly-compressible SPH scheme. We employ the method of manufactured solutions to systematically develop the scheme and validate the solver. We demonstrate the order of convergence of the entire scheme using the Taylor-Green vortex problem and then go on to demonstrate the applicability of the method to simulate flow past a circular cylinder.

*Keywords:* Second-order, Adaptive resolution, SPH, weakly-compressible

---

---

\*Corresponding author

*Email addresses:* [pawan.n@aero.iitb.ac.in](mailto:pawan.n@aero.iitb.ac.in) (Pawan Negi),  
[prabhu@aero.iitb.ac.in](mailto:prabhu@aero.iitb.ac.in) (Prabhu Ramachandran)

<sup>1</sup>Joint first author

## 1. Introduction

<sup>2</sup> The smoothed particle hydrodynamics (SPH) method is a Lagrangian, meshless method widely used to simulate continuum mechanics problems including fluid dynamics [1, 2, 3] and elastic dynamics [4, 5]. The meshless nature of the method inherently allows adaptivity of the particles according to the dynamics of the specific problem. However, there are still several challenges [6] to overcome for SPH to emerge as a reliable equivalent to traditional mesh-based methods applied in industry.

As discussed by Vacondio et al. [6], a second-order convergent Lagrangian SPH scheme is a grand-challenge problem. The root cause of non-convergence is the selection of a non-convergent (but conservative) discretization method [7]. In SPH, a discretization that is both convergent and conservative is not available [8, 7]. Therefore, one has to choose between a conservative or a convergent discretization. According to Price [8], conservation is important, furthermore it provides inherent particle regularization. However, Negi and Ramachandran [7] show that in the case of incompressible and weakly-compressible fluids, the linear momentum remains bounded (though not conserved) when one uses a convergent scheme and the accuracy achieved is very high. Along similar lines, many authors [9, 10, 7, 11, 12] have proposed convergent techniques that are not conservative. In order to construct a second-order convergent scheme, a kernel gradient correction [13, 14] of some form is necessary and this can be computationally expensive.

Traditional SPH schemes for incompressible or weakly-compressible fluids have tended to employ a fixed resolution of particles wherein all particles are of the same spatial resolution. As can be expected, this is highly inefficient especially in the case of fluid dynamics where high-resolution is only necessary in certain regions. As a result, many adaptive resolution schemes have been proposed over the years where the particle resolution is adaptively refined.

Feldman and Bonet [15] proposed a dynamic refinement strategy ensuring mass conservation. They ensured that the global kinetic energy, linear momentum, and angular momentum are conserved by the method. Vacondio et al. [16, 17] developed this further and proposed a splitting as well as a merging technique ensuring corrections due to variable particle resolution. Barcarolo et al. [18] proposed to retain the parent particle after splitting to use it as

---

<sup>2</sup>© 2024. This manuscript version is made available under the CC-BY-NC-ND 4.0 license <https://creativecommons.org/licenses/by-nc-nd/4.0/>

a support while merging. Chiron et al. [19] improved the adaptive particle refinement proposed by Vacondio et al. [20, 21]. Their proposed method resolved issues due to particles of different sizes interacting and retained the parent and child particles in the region between two different resolutions. Sun et al. [22, 23, 24] also used this approach with a buffer region between two distinct particle resolutions. Two different resolution do not interact while computing the accelerations. Recently, Ricci et al. [25] used a similar approach to decompose the domain into different layers that interact through buffer layers. Yang and Kong [26, 27] proposed a dynamic strategy to set the smoothing length that allowed a continuous variation of the smoothing length from minimum to maximum resolution in the domain. Recently, Muta and Ramachandran [28], followed by an improvement in Haftu et al. [29], proposed a parallel implementation that combines the approaches of Vacondio et al. [21] along with that of Yang and Kong [27]. The method is accurate, has optimal smoothing lengths, requires much fewer particles than other schemes, does not require a manual specification of spatial resolution, and also fully supports object motion and solution adaptivity. We note that none of the methods discussed require a support mesh to determine the particle resolutions. While these methods allows accurate solutions to the shallow water equations [16], soil simulation [30], fluid mechanics problems [29], fluid-structure interaction [31] and multi-phase simulations [27]. However, none of the above methods are second-order accurate. As mentioned earlier, this is a grand-challenge problem.

In this paper, we propose a second-order convergent (SOC) adaptive refinement strategy and a SOC scheme for variable smoothing length particles. We develop the method in two parts. We first develop a SOC scheme for variable smoothing length. We use the first-order consistency correction for the kernel gradients in the approximation of all the operators. This ensures correct estimation of the property irrespective of the smoothing length variation. We use particle shifting technology (PST) [32] to iteratively shift particle after every few iterations. We use the method of manufactured solutions (MMS) as proposed in [12] to ensure that the new scheme is indeed SOC in the presence of variable smoothing length.

In the second part, we use the adaptive refinement strategy proposed by Haftu et al. [29]. The adaptive strategy consist of three parts where the field properties are updated, namely, particle splitting, particle merging, and shifting. We propose a second-order convergent approximation for each of these updates and use the original algorithm as is. Once again, we use the

MMS to show that the adaptive refinement strategy is indeed SOC.

In the next section, we briefly discuss the SPH method and the types of approximation that works in the presence of variable smoothing length,  $h$ . In section 3, we discuss the second-order scheme followed by the second-order convergent adaptive refinement strategy. We discuss the original algorithm that we do not change in the Appendix A. In section 4, we demonstrate the accuracy of the proposed method by simulating Taylor-Green vortex and the flow past a circular cylinder. In the interest of reproducibility we automate [33] the results of this work. The entire source-code of the work conducted in this paper can be found at [https://gitlab.com/pypr/adaptive\\_mms](https://gitlab.com/pypr/adaptive_mms).

## 2. The SPH method

In the SPH method [34], the scalar field  $f$  defined in the domain  $\Omega$  with boundary  $\partial\Omega$  is reconstructed (away from the domain boundary), with second-order accuracy, using a smoothing kernel  $W$  as

$$f(\mathbf{x}) = \int_{\Omega} f(\tilde{\mathbf{x}})W(\mathbf{x} - \tilde{\mathbf{x}}, h)d\tilde{\mathbf{x}} + O(h^2), \quad (1)$$

where  $\mathbf{x} \in \Omega$  and  $h$  is the smoothing length of the kernel. Similarly, the gradient of the scalar field

$$\nabla f(\mathbf{x}) = \int_{\Omega} f(\tilde{\mathbf{x}})\nabla W(\mathbf{x} - \tilde{\mathbf{x}}, h)d\tilde{\mathbf{x}} + O(h^2). \quad (2)$$

The domain can be discretized using particles having uniform mass and constant smoothing length. Using discrete particles, the SPH discretization of the function gradient

$$\nabla f(\mathbf{x}_i) = \sum_{j=1}^N f(\mathbf{x}_j)\nabla W_{ij}\omega_j + E_{\text{quad}} + O(h^2), \quad (3)$$

where  $E_{\text{quad}}$  is the quadrature error [35],  $\omega_j$  is the volume of the particle,  $\nabla W_{ij} = \nabla_i W(\mathbf{x}_i - \mathbf{x}_j, h_{ij})$ , and the sum is taken over  $N$  neighbors of the particle  $i$ . We note that it is possible to employ a distribution of particles with variable mass  $m$  and variable smoothing length  $h$ . Vacondio et al. [17] proposed a formulation to evaluate the gradient of a scalar field to account for the variation of  $h$  as

$$\langle \nabla f(\mathbf{x}_i) \rangle = \sum_j m_i m_j \left( \frac{f_j}{\beta_j \rho_j^2} \nabla W_j - \frac{f_i}{\beta_i \rho_i^2} \nabla W_i \right), \quad (4)$$

where,

$$\beta_i = -\frac{1}{\psi_i d} \sum_j m_j \mathbf{x}_{ij} \nabla W_{ij}, \quad (5)$$

is the correction term due to the variation in  $h$ ,  $\psi_i$  is the particle density,  $d$  is the dimension of the problem,  $\mathbf{x}_{ij} = \mathbf{x}_i - \mathbf{x}_j$ , and  $\nabla W_i = \nabla W(\mathbf{x}_i - \mathbf{x}_j, h_i)$ . The formulation in eq. (4) conserves linear momentum pair-wise. In the context of the SPH method, many researchers [8, 7] have shown that a formulation that is conservative and second-order convergent is not available. Recently, Sun et al. [36], Lüthi et al. [37], Pearl et al. [38] employed kernel gradient correction to correctly evaluate gradients in the presence of variable resolution. Using a similar technique, we propose a second-order convergent gradient estimation, in the presence of variable resolution,

$$\langle \nabla f(\mathbf{x}_i) \rangle = \sum_j f_j \nabla \tilde{W}_j \omega_j, \quad (6)$$

where  $\nabla \tilde{W}_j = L_i \nabla W(\mathbf{x}_i - \mathbf{x}_j, h_j)$  is the corrected kernel gradient, where  $L_i$  is the first order correction matrix proposed by Liu and Liu [14] and discussed in greater detail in section 3.1. In the next section, we extend this formulation and propose a second-order convergent scheme for an adaptively refined domain.

### 3. A second-order convergent scheme for variable $h$

The time-accurate simulation of an incompressible fluid can be performed using the weakly-compressible Navier-Stokes (N-S) [39] equations

$$\begin{aligned} \frac{d\rho}{dt} &= -\rho \nabla \cdot \mathbf{u}, \\ \frac{d\mathbf{u}}{dt} &= -\frac{\nabla p}{\rho} + \nu \nabla^2 \mathbf{u}, \end{aligned} \quad (7)$$

where  $\rho$  and  $\nu$  are the fluid density and kinematic viscosity, respectively. The above equation is closed using an artificial equation of state

$$p = c_o^2(\rho - \rho_o), \quad (8)$$

where  $c_o$  is the artificial speed of sound and  $\rho_o$  is the reference density. Using the equation of state and the entropically damped artificial compressibility

(EADC) approach [40, 41, 2], the continuity equation can be written as a pressure evolution equation

$$\frac{dp}{dt} = -\rho c_o^2 \nabla \cdot \mathbf{u} + D \nabla^2 p, \quad (9)$$

where  $D = \alpha h c_o / 8$  is the density damping coefficient, where is recommended to be  $\alpha = 0.5$  [2].

In this work, we extend the existing scheme proposed by Muta and Ramachandran [28] using the pressure evolution eq. (9) along with the momentum equation to simulate fluid flows. However, we may also choose to use a density evolution equation and this has no impact on the convergence of the method as demonstrated in [7]. We divide the construction of the proposed scheme in two stages. We first propose a SOC scheme in the presence of variable resolution. We use a particle shifting technique [32] to ensure uniform particle distribution with an accurate Taylor series correction. In the subsequent stage, we add a SOC splitting and merging to the scheme. At each stage, we use the method of manufactured solutions proposed by Negi and Ramachandran [12] to verify the convergence. We employ the techniques proposed in [7] to construct the discrete operators. The boundary (solid, inlet, outlet) particles have the same resolution as the nearby fluid particle. Therefore, we can directly apply the convergent boundary condition implementation identified in [11]. In the next section, we describe the construction of a second-order convergent EDAC scheme.

### 3.1. Second-order EDAC scheme

Negi and Ramachandran [7] proposed a SOC scheme with pressure evolution for a uniform resolution. However, in the case of variable resolution, a straight-forward implementation does not work despite the use of a kernel gradient correction. In the presence of variable resolution, we set the particle volume  $\omega$  and the corresponding smoothing length  $h$  such that the summation density  $\psi$  produces the desired reference particle density, which in this work is set to 1. We set the  $h$  of a particle using

$$h_i = C \left( \frac{m_{avg}}{\psi_o} \right)^{1/d}, \quad (10)$$

where  $m_{avg} = \sum_j m_j / N$ ,  $C = 1.2$ ,  $d$  is the dimensionality of the problem,  $\psi_o = 1$  is the desired particle density (or summation density). In the case of

variable smoothing length, there are two different ways to compute volume namely, scatter and gather formulation [42]. Muta and Ramachandran [28] proposed to use gather formulation to compute volume

$$\omega_i = \frac{1}{\sum_j W((x_i) - \mathbf{x}_j, h_i)} = \frac{1}{\sum_j W_i}. \quad (11)$$

We use eq. (6) to obtain the discretization of the continuity equation

$$\frac{dp_i}{dt} = -\rho_i c_0^2 \sum_j \mathbf{u}_j \cdot \nabla \tilde{W}_j \omega_j + \frac{\alpha h_i c_0}{8} \sum_j (p_j - p_i) \frac{\mathbf{x}_{ij} \cdot \nabla \tilde{W}_j}{|\mathbf{x}_{ij}| + 0.01 h_j^2} \omega_j \quad (12)$$

where  $\nabla \tilde{W}_j = L_i \nabla W_j$ , and the correction matrix  $L_i$  is obtained by solving

$$\begin{bmatrix} \sum_j W_j \omega_j & \sum_j \mathbf{x}_{ji} W_j \omega_j \\ \sum_j \mathbf{x}_{ji} W_j \omega_j & \sum_j (\mathbf{x}_{ji} \otimes \mathbf{x}_{ji}) W_j \omega_j \end{bmatrix} \begin{bmatrix} \tilde{W}_i \\ \nabla \tilde{W}_i \end{bmatrix} = \begin{bmatrix} W_i \\ \nabla W_i \end{bmatrix}. \quad (13)$$

We note that the construction of the correction matrix also involves one-sided kernel function values. The second term in eq. (12) is a discretization proposed by [43] for the Laplacian term. We do not employ a discretization using a repeated application of the SOC gradient and divergence operator as it is unstable in the presence of oscillations [44]. However, the presence of the  $h_i$  in the damping term makes the error due to the non-convergent discretization at least first order.

We use a similar discretization for the momentum equation

$$\frac{d\mathbf{u}_i}{dt} = -\frac{1}{\rho_i} \sum_j p_j \nabla \tilde{W}_j \omega_j + \nu \sum_j \langle \nabla u_i \rangle \cdot \nabla \tilde{W}_j \omega_j, \quad (14)$$

where  $\langle \nabla u_i \rangle = \sum_j \mathbf{u}_j \otimes \nabla \tilde{W}_j \omega_j$  is the SOC velocity gradient. The discretized equations eqs. (12) and (14) are integrated in time using the second-order Runge-Kutta method. The details of the integrator can be found in [7].

We use the method of manufactured solutions [12] to demonstrate the second-order convergence of the scheme keeping a uniform resolution. The manufactured solution (MS) used is given by

$$\begin{aligned} u(x, y) &= (y - 1) \sin(2\pi x) \cos(2\pi y), \\ v(x, y) &= -\sin(2\pi y) \cos(2\pi x), \\ p(x, y) &= \cos(4\pi x) + \cos(4\pi y). \end{aligned} \quad (15)$$

By putting the MS in the governing equation in eqs. (7) and (9) with  $\nu = 0$  and  $\alpha = 0$ , we obtain a source term for momentum and pressure evolution. The resulting source term is passed to the solver. Since, both the viscous term and the pressure damping term is zero, the error is only due to the discretized velocity divergence and pressure gradient operators. In fig. 1, we plot the  $L_1$  error in pressure and velocity after 1 time step for the proposed scheme with the change in average particle spacing  $\Delta s$ . The rate of convergence is clearly second-order.

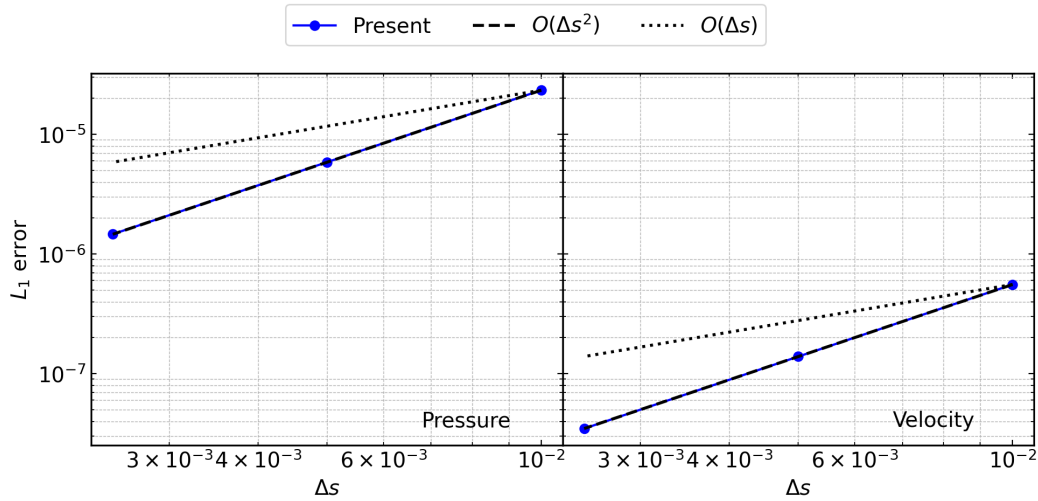


Figure 1:  $L_1$  error in pressure and velocity after 1 time step using the MS in eq. (15) with  $\alpha = 0$  and  $\nu = 0$ .

We note that the result in fig. 1 demonstrates that the error may not originate from the velocity divergence and pressure gradient approximation. In order to test the accuracy of the discretization of the pressure damping and velocity damping (or the viscous term), we use the MS given by

$$\begin{aligned}
 u(x, y, t) &= (y - 1) e^{-10t} \sin(2\pi x) \cos(2\pi y), \\
 v(x, y, t) &= -e^{-10t} \sin(2\pi y) \cos(2\pi x), \\
 p(x, y, t) &= (\cos(4\pi x) + \cos(4\pi y)) e^{-10t}.
 \end{aligned} \tag{16}$$

We evaluate the source term by setting  $\nu = 0.25$  and  $\alpha = 0.5$  in the governing equation. In fig. 2, we plot the  $L_1$  error for pressure and velocity after 1 time step. A slight deviation from the second-order rate of convergence is



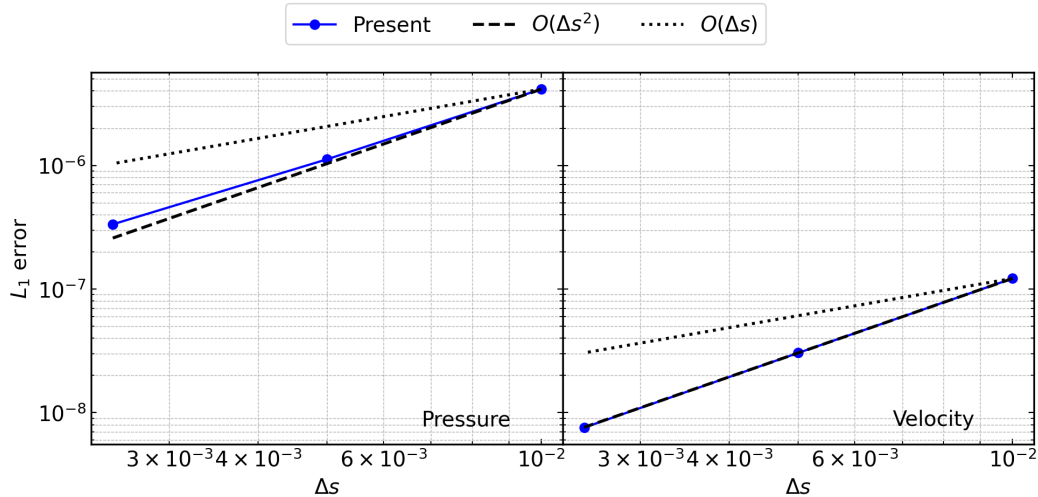


Figure 2:  $L_1$  error in pressure and velocity after 1 time step using the MS in eq. (16) with  $\alpha = 0.5$  and  $\nu = 0.25$ .

visible. It is due to the non-convergent discretization employed in the pressure gradient term to mitigate pressure oscillations.

In order to test the convergence of the proposed scheme in the presence of variable resolution, we consider domain with variable resolution as shown in fig. 3. We consider a patch with a doubled particle resolution at the middle of the original uniform particle distribution. We also consider the patch having non-uniform, packed distribution. In order to perform a convergence study, we reduce the resolution by half for all particles.

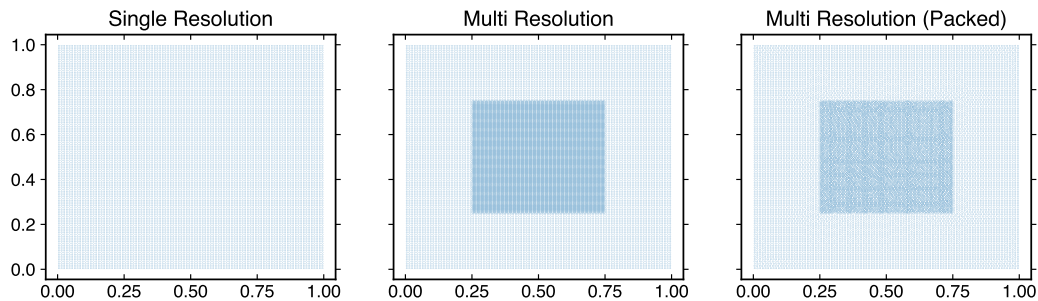


Figure 3: Different particle resolution considered.

In fig. 4, we plot the  $L_1$  error for pressure and velocity after 100 time steps. The proposed scheme demonstrates second-order convergence in the

presence of variable resolution and different particle distributions.

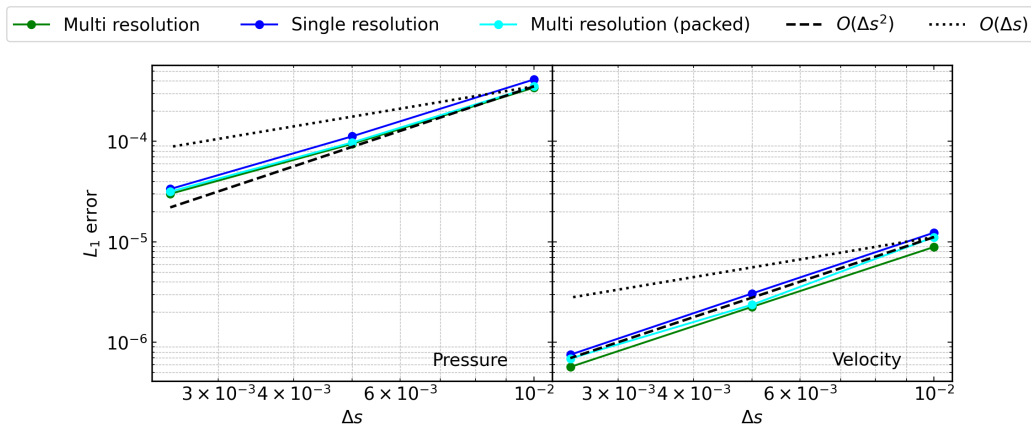


Figure 4:  $L_1$  error in pressure and velocity after 100 time steps using the MS in eq. (16) with  $\alpha = 0.5$  and  $\nu = 0.25$ .

### 3.2. Second-order splitting and merging

In this section, we modify the original splitting and merging technique proposed by Muta and Ramachandran [28] to ensure a second-order convergent property update for the newly created particles. This enables the present scheme to remain SOC along with the particle splitting and merging. However, the proposed idea is applicable to any adaptive particle refinement method [17, 27]. For brevity, we refer to [28] as MAPR (abbreviated for Muta et al. (2022) Adaptive Particle Refinement) in this discussion. We discuss the proposed modification here and the complete algorithm is elaborated in Appendix A. In the next sub-section, we first discuss the particle splitting technique.

#### 3.2.1. Splitting a particle

In MAPR, one particle of mass  $m$  is split into seven child particles. The mass of all the particles is set equal to  $m/7$ . The properties like velocity and pressure of the child particles are set equal to the parent particle. However, in this work we propose to perform Taylor series correction to determine the property value. Assuming that the particle represents a scalar field  $\phi$ , a new particle  $\mathbf{x}_{sp}$  away from the parent particle uses the first order Taylor-series correction such that

$$\phi(\mathbf{x}_s) = \phi(\mathbf{x}_p) + \mathbf{x}_{sp} \cdot \langle \nabla \phi(\mathbf{x}_p) \rangle, \quad (17)$$

where  $\mathbf{x}_{sp} = \mathbf{x}_s - \mathbf{x}_p$  is the displacement of child particle  $s$  from the parent particle  $p$ , and  $\langle \nabla \phi(\mathbf{x}_p) \rangle$  is the gradient of the property computed on the parent particle. This gradient should be computed before the splitting/merging is performed. This is essential because the original particle distribution represents the original field variable and can be used to evaluate second-order accurate gradients.

### 3.2.2. Iterative Shifting while splitting/merging

In MAPR, the particles are iteratively shifted in order to make the particles uniform while splitting and primarily while merging (see algorithm in Appendix A). We use the shifting technique proposed in [32]. The shift vector

$$\delta \mathbf{x}_i = \frac{0.5h_i^2}{\beta_i} \sum_j \left( 1 + 0.2 \left( \frac{W_j}{W(\Delta s)} \right)^4 \right) \frac{m_j}{\psi_o} \nabla W_j, \quad (18)$$

where  $W(\Delta s)$  is the smoothing kernel value with the average particle spacing. We correct the shift vector using the  $\beta_i$  term to accommodate the effect of the change of smoothing length. We note that a kernel gradient correction should not be employed. We iteratively shift the particles to a prescribed number of times (thrice in the current work) and correct the properties using the Taylor series correction such that any property

$$\phi(\mathbf{x}_i + \delta \mathbf{x}_i) = \phi(\mathbf{x}_i) + \delta \mathbf{x}_i \cdot \langle \nabla \phi(\mathbf{x}_i) \rangle, \quad (19)$$

where  $\langle \nabla \phi(\mathbf{x}_i) \rangle$  is the gradient computed before the start of the splitting/merging process.

### 3.2.3. Merging particles

In MAPR, merging is performed multiple times in a single split/merge cycle to enable parallel processing. We note that at a time only two particles merge to become one and a next set of particles are marked for merging afterwards. In MAPR, the position of the merged particle  $\mathbf{x}_m$  is set as

$$\mathbf{x}_m = \frac{m_a \mathbf{x}_a + m_b \mathbf{x}_b}{m_m}, \quad (20)$$

where  $m_m = m_a + m_b$  is the mass of the merged particle. The velocity or pressure of the particle is set as

$$\phi_m = \frac{m_a \phi_a + m_b \phi_b}{m_m}. \quad (21)$$

However, we note that the original particles represent a scalar field  $\phi$  and the resulting merged particle must represent the same field. Therefore, the property value using a first-order Taylor series approximation from the nearest particle  $n$  to the new merged location,

$$\phi(\mathbf{x}_m) = \phi(\mathbf{x}_n) + \mathbf{x}_{mn} \cdot \langle \nabla \phi(\mathbf{x}_n) \rangle, \quad (22)$$

where  $\langle \nabla \phi(\mathbf{x}_n) \rangle$  is the gradient evaluated before the merging cycle begins.

One adaptive refinement cycle may consist of multiple merges, we demonstrate the approximation for the scenarios where the merge is performed between two newly split particles  $s_1$  and  $s_2$ . The property at those particles are

$$\phi(\mathbf{x}_{s_1}) = \phi(\mathbf{x}_{p_1}) + \mathbf{x}_{s_1 p_1} \cdot \langle \nabla \phi(\mathbf{x}_{p_1}) \rangle, \quad (23)$$

and

$$\phi(\mathbf{x}_{s_2}) = \phi(\mathbf{x}_{p_2}) + \mathbf{x}_{s_2 p_2} \cdot \langle \nabla \phi(\mathbf{x}_{p_2}) \rangle, \quad (24)$$

where  $p_1$  and  $p_2$  are the parent particle. Let us assume  $p_1$  is closer to the merged location, thus the property for the new merged particle is given by

$$\phi(\mathbf{x}_m) = \phi(\mathbf{x}_{s_1}) + \mathbf{x}_{m s_1} \cdot \langle \nabla \phi(\mathbf{x}_{p_1}) \rangle, \quad (25)$$

From eq. (23), we get

$$\begin{aligned} \phi(\mathbf{x}_m) &= \phi(\mathbf{x}_{p_1}) + \mathbf{x}_{s_1 p_1} \cdot \langle \nabla \phi(\mathbf{x}_{p_1}) \rangle + \mathbf{x}_{m s_1} \cdot \langle \nabla \phi(\mathbf{x}_{p_1}) \rangle \\ &= \phi(\mathbf{x}_{p_1}) + \mathbf{x}_{m p_1} \cdot \langle \nabla \phi(\mathbf{x}_{p_1}) \rangle \end{aligned} \quad (26)$$

In a similar manner, we can show that the particle created from a merged particle maintains a first-order Taylor-series approximation centered at chosen nearest parent particle. Hence, the proposed merging is second-order accurate. We note that we copy the gradient values of the parent particle to the child particles. In the next section, we apply the proposed scheme to simulate real flows.

#### 4. Results and discussion

In this section, we simulate two test cases viz. the Taylor-Green vortex and flow past a circular cylinder. We compare the results obtained with the adaptive SPH scheme proposed by Muta and Ramachandran [28] and other established methods in the literature.

#### 4.1. Taylor-Green Vortex

The Taylor-Green vortex is an incompressible flow with an exact solution given by

$$\begin{aligned} u(x, y, t) &= -U \exp(bt) \cos(2\pi x) \sin(2\pi y), \\ v(x, y, t) &= U \exp(bt) \sin(2\pi x) \cos(2\pi y), \\ p(x, y, t) &= -0.25 U^2 \exp(2bt) \cos(2\pi x) \cos(2\pi y), \end{aligned} \quad (27)$$

where  $b = -8\pi^2/Re$ , and  $Re = UL/\nu$  is the Reynolds number of the flow. For the simulation, we consider a square domain of  $L = 1$  m and maximum velocity  $U = 1.0$   $\text{ms}^{-1}$ . We set the viscosity  $\nu = UL/Re$  and the artificial speed of sound  $c_o = 20$   $\text{ms}^{-1}$ . We simulate the problem at the Reynolds numbers 100 and 1000. We consider a patch of fluid in the middle of the domain which has exactly half of the particle spacing of the larger domain. We simulate the flow for  $t = 2$  s.

In fig. 5, we plot the smoothing length variation and pressure in the domain at  $t = 2$  s for the  $Re = 1000$  case. The pressure plot does not show any error originating at the interface of different resolutions.

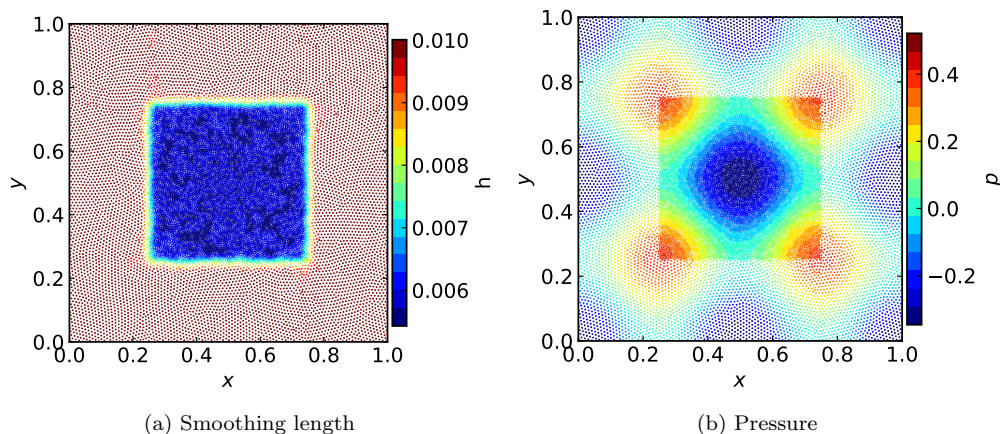


Figure 5: Smoothing length variation and pressure at  $t = 2.0$  s for  $Re = 1000$ .

In fig. 6, we show the kinetic energy dissipation for the Taylor-Green vortex and compare the results with that of Chiron et al. [19]. The results of the present scheme are shown with 5 different resolutions, viz.  $N = 50, 80, 100, 160,$  and  $200$ , where the parameter  $N$  is the number particles along the  $x$ -direction. The obtained results are very close to the expected exact dissipation rate and are significantly better than those of Chiron et al. [19].

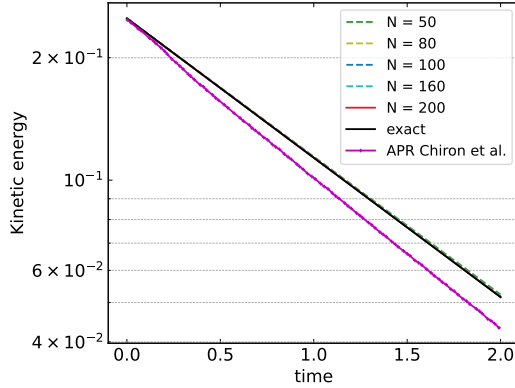


Figure 6: Kinetic energy dissipation of the Taylor-Green vortex for different resolutions compared with the exact solution and the results of Chiron et al. [19].  $N$  represents the number of particles along  $x$ -direction indicating the resolution.

In fig. 7, we plot the convergence in velocity and pressure for the present method and compare it with the convergence of the results in Muta and Ramachandran [28]. Both velocity and pressure shows second order convergence. Compared to the results of [28], the errors are an order of magnitude lower. Furthermore, convergence in pressure is entirely absent in their scheme.

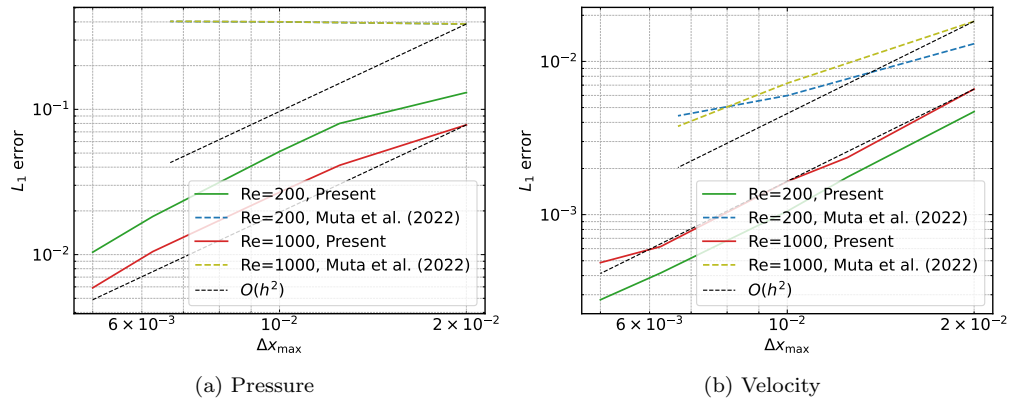


Figure 7: Comparison of the  $L_1$  error in pressure for the adaptive scheme of [28] and the present scheme.

#### 4.2. Flow past a circular cylinder

The flow past a circular cylinder is a widely used benchmark problem. It is simple but at the same time exhibits complex flow physics. In this test case,

we consider a two-dimensional circular cylinder of diameter  $D = 2$  m. The free-stream velocity  $U$  is set to  $1 \text{ ms}^{-1}$ . However, the desired Reynolds number is attained by setting the kinematic viscosity  $\nu = UD/Re$ . We consider a uniform particle resolution across the boundaries i.e. wall, inlet, outlet and the cylinder. Therefore, the boundary condition implementations suggested in [11] can be readily applied to achieve second-order convergence. We apply the boundary condition implementation proposed by [45] for pressure, slip and no-slip boundary condition. For the inlet and outlet, we employ the method in [46] for the non-reflection of the pressure waves. However, in the case where the reference properties like mean velocity and pressure are unknown, the method in [47] can be employed. We also apply non-reflection condition at the far-field inviscid wall.

In fig. 8, we show the comparison of particle distribution around the cylinder for the simulation of  $Re = 9500$  for the present case and the one considered in [28]. We obtain a rapid change in the particle resolutions due to the improved algorithm in [29] resulting in a significant reduction of the total number of particles in the domain. Furthermore, in table 1, we show the total number of particles at the highest resolution for different Reynolds numbers.

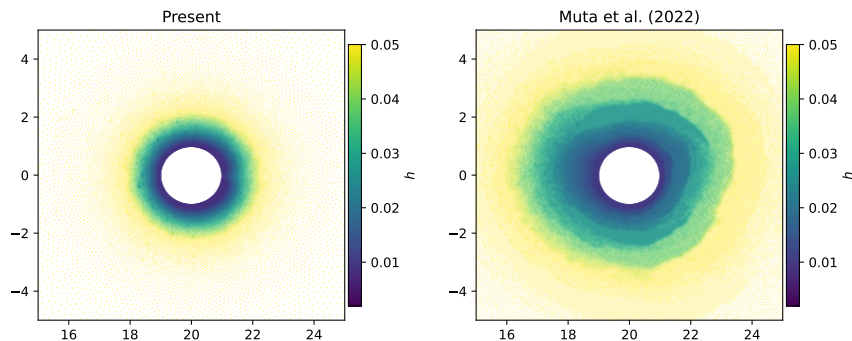


Figure 8: Comparison of the variation of particle resolution near the cylinder between the present work and [28].

For every case, the cylinder is resolved at the highest resolution,  $\Delta s_{\min}$ , whereas the inlet/outlet and the wall particles are set at the lowest resolution  $\Delta s_{\max} = 0.5$ . In this work we have considered three different highest resolutions for the cylinder namely,  $D/\Delta s_{\min} = 100, 200, 500$ , while keeping a fixed  $\Delta s_{\max}$ . The growth constant  $c_r = 1.15$ . Additionally, we employ

Re	$C_r$	$D/\Delta s_{min}$	Number of particles	
			Muta et al. (2022) [28]	Present
40	1.08	500	203k	137k
550	1.08	500	193k	92k
1000	1.08	500	215k	89k
3000	1.08	500	212k	81k
9500	1.15	1000	196k	141k

Table 1: Comparison of the total number of particles in the present method as against that of Muta and Ramachandran [28] at the highest resolution at different Reynolds numbers.

solution adaptivity based on vorticity magnitude to refine the vortices as they develop. For the  $Re = 9500$  case, we also employ a highest resolution of  $D/\Delta s_{min} = 1000$ . We demonstrate the qualitative accuracy across the resolution for the  $Re = 9500$  case alone.

In fig. 9, we plot the vorticity at  $t = 3$  s and 6 s. The vorticity field shows no jump or variation due to the presence of different resolution particles in the vicinity of the solid.

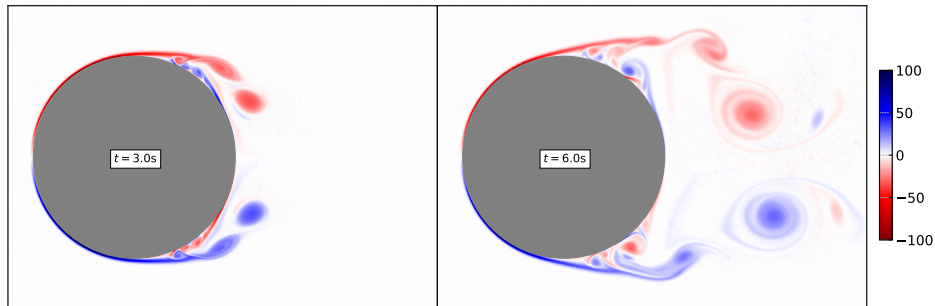


Figure 9: Vorticity distribution for  $Re = 9500$  at  $t = 3$  s and 6 s.

In fig. 10, we plot the pressure variation around the cylinder at  $t = 3$  s and 6 s. Similar to vorticity distribution, the pressure also does not show any variation due to the change in smoothing length. Additionally, the pressure remains around  $100Pa$  which is the reference pressure. It shows that the pressure remains bounded as expected for a weakly-compressible scheme.

To perform a quantitative comparison, we compute the skin-friction and pressure drag. To compute the skin-friction drag force  $f_{sf}$ , we compute the volume integral of the viscous force in the volume  $\Omega$  defined by the boundary



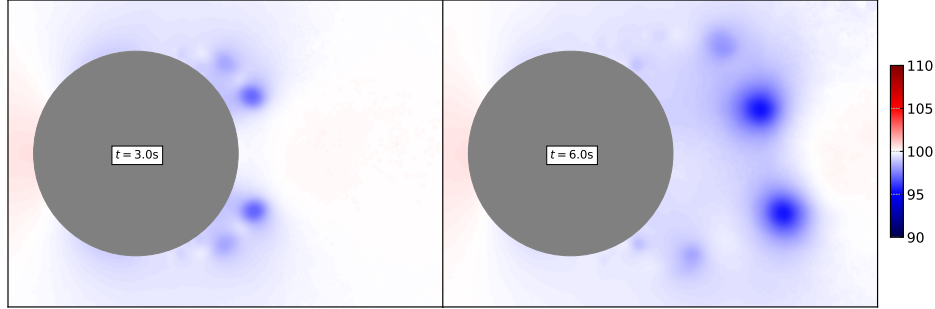


Figure 10: Pressure distribution for  $Re = 9500$  at  $t = 3$  s and 6 s.

of the cylinder, which is defined for a given dynamic viscosity  $\mu$  as

$$\mathbf{f}_{sf} = \int_{\Omega} \mu \nabla^2 \mathbf{u} d\mathbf{x}. \quad (28)$$

Using the divergence theorem, we can write

$$\mathbf{f}_{sf} = \int_{\partial\Omega} \mu \nabla \mathbf{u} \cdot \mathbf{n} dS(\mathbf{x}) \approx \sum_{i=1}^N \mu \langle \nabla \mathbf{u} \rangle_i \cdot \mathbf{n}_i S(\mathbf{x}_i), \quad (29)$$

where  $S(\mathbf{x})$  is surface area function,  $\mathbf{n}$  is the outward normal,  $\langle \nabla \mathbf{u} \rangle_i$  is the SPH approximation of the velocity gradient computed during the simulation. The boundary of the cylinder is discretized into  $N$  equal elements. The skin-friction drag coefficient is evaluated using the  $x$ -component of the computed force divided by  $\frac{1}{2}\rho_o U^2$ .

In fig. 11, we plot the skin-friction drag for the cylinder. The computed skin-friction drag closely follows the results in [48, 49] as well as the adaptive SPH method of Muta and Ramachandran [28].

In a similar manner, pressure drag force  $\mathbf{f}_{pf}$  is computed using the force due to pressure gradient in the volume defined by the boundary of the cylinder, which is given by

$$\mathbf{f}_{pf} = \int_{\Omega} \nabla \cdot (p\mathbf{I}) d\mathbf{x}, \quad (30)$$

where  $\mathbf{I}$  is an identity matrix. Using the divergence theorem, we can write

$$\mathbf{f}_{pf} = \int_{\partial\Omega} p\mathbf{I} \cdot \mathbf{n} dS(\mathbf{x}) \approx \sum_i^N \langle p \rangle_i \mathbf{I} \cdot \mathbf{n}_i S(\mathbf{x}_i), \quad (31)$$

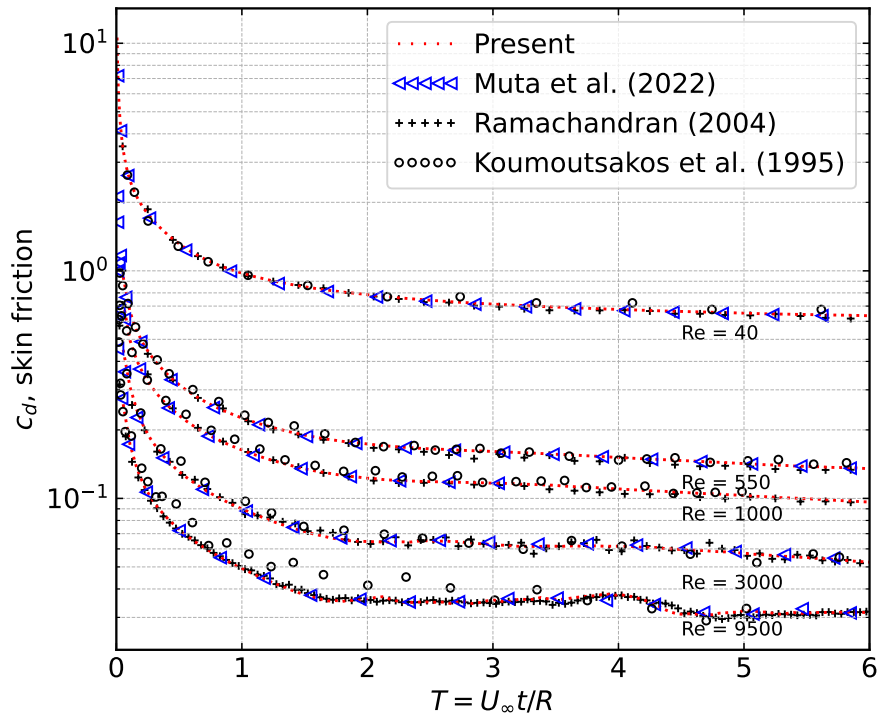


Figure 11: Skin-friction drag history for different Reynolds numbers compared with [48, 49, 28].

where  $\langle p \rangle_i$  is the pressure evaluated using SPH approximation. The pressure drag coefficient is evaluated by dividing the  $x$ -component with  $\frac{1}{2}\rho_o U^2$ .

In fig. 12, we plot the pressure drag coefficient for  $Re = 40, 550, 1000,$  and  $3000$  across different resolutions. We note that the higher Reynolds number flows behave poorly at lower resolution. However, at resolution  $D/\Delta s_{min} = 500$  all the cases match those presented in the literature.

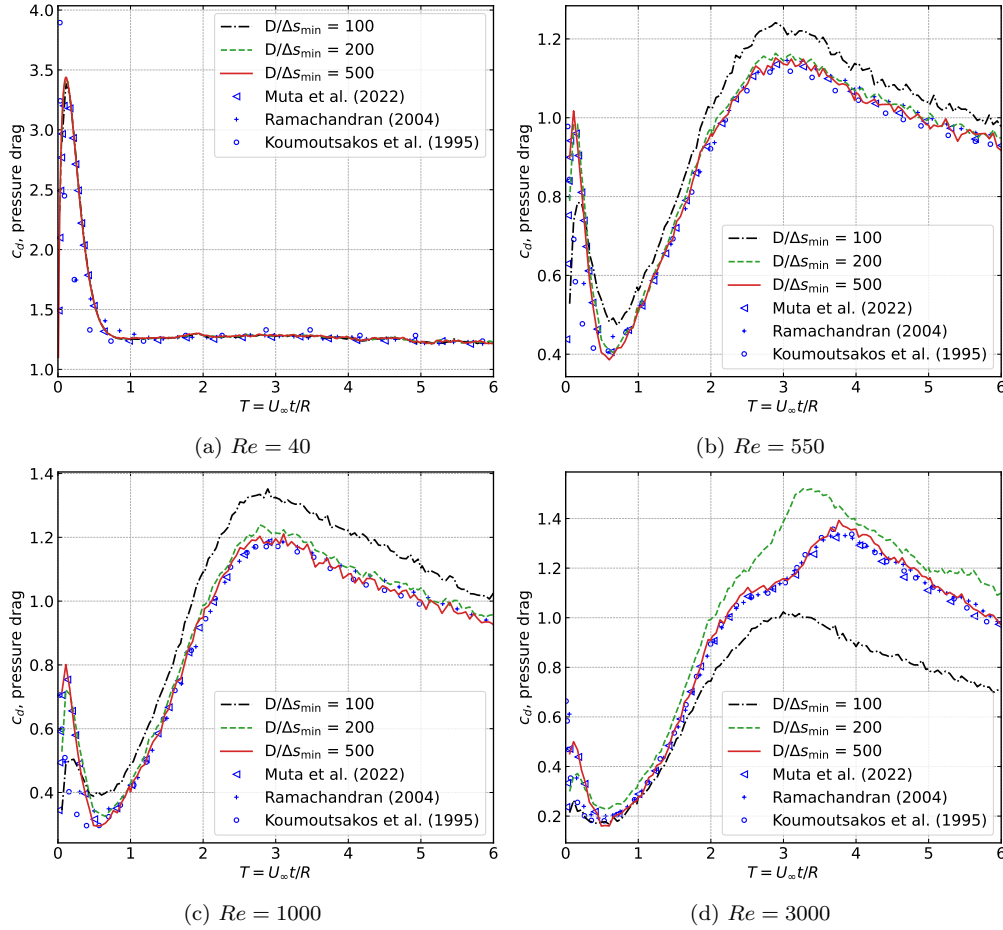


Figure 12: Coefficient of pressure drag history for different resolutions compared with the results in [48, 49, 28].

In fig. 13, the  $Re = 9500$  case, a further increment in the highest resolution to  $D/\Delta s_{min} = 1000$  is required to properly capture the pressure drag. We also use a  $C_\tau$  value of 1.15 to increase the rate of change of resolution hence,

decreasing the total number of particles. This also demonstrates that the proposed method works with much rapid change in resolution.

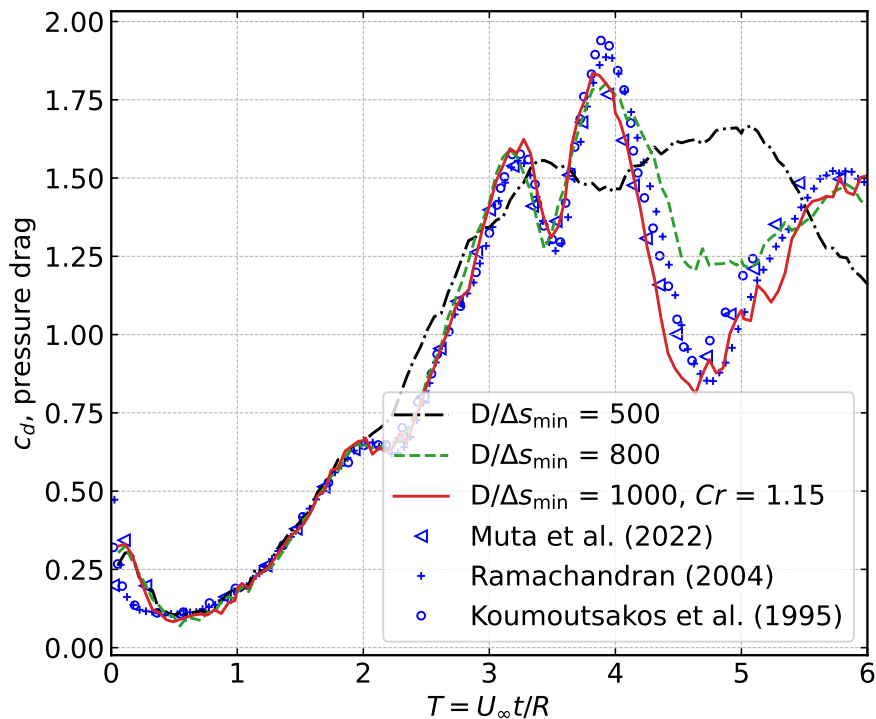


Figure 13: Coefficient of pressure drag history for  $Re = 9500$  for different resolutions compared with the results in [48, 49, 28].

## 5. Conclusions

In this study, we propose a second-order convergent, weakly-compressible scheme for adaptive resolution SPH. We propose to employ a second-order kernel gradient correction in the presence of variable resolution to accurately evaluate the gradient, divergence and Laplacian of a scalar field. More importantly, the SPH operator discretizations and the kernel correction matrices must consistently use one-sided kernel,  $W_i = W(\mathbf{x}_{ij}, h_i)$ , to ensure first-order consistency. We also demonstrate successful application of the method of manufactured solution to verify the second-order convergence of the proposed scheme during the development. To maintain second-order accuracy while adaptively splitting and merging of particles, we employ a

Taylor series correction to consistently update the properties. We emphasise to compute property gradients before the split/merge process. Using the Taylor-Green vortex problem, we demonstrate the convergence and accuracy of the proposed scheme. We simulate the flow past a circular cylinder to demonstrate the accuracy of skin friction and pressure-drag while using a significantly lower total number of fluid particles. In the future, we plan to extend the method to free-surface and multiphase flow problems.

## Appendix A. Adaptive splitting and merging algorithm

In this section, we highlight the differences and describe the particle splitting and merging algorithm proposed by [28, 29] for the sake of completeness. As mentioned in section 3.2, the splitting and merging processes are not changed in the present method.

The initialization of the fluid particles before the start of the simulation is described in [29]. However, any other method to generate a adaptive particle distribution is supported and does not effect the described SOC algorithm.

In algorithm 1, we determine the resolution level  $h_{\text{tmp}}$  for a particle. For each particle, we compute three quantities viz.  $\Delta s_{\text{max}}$ ,  $\Delta s_{\text{min}}$ , and geometric average spacing  $\Delta s_{\text{avg}}$  in its neighborhood. For a particle, if the ratio  $\frac{\Delta s_{\text{max}}}{\Delta s_{\text{min}}} < (C_r)^3$  (where,  $C_r$  is the prescribed rate of change of resolution), then it is resolved further to  $\min(\Delta s_{\text{max}}, C_r \Delta s_{\text{min}})$  otherwise the new resolution is set as the current  $\Delta s_{\text{avg}}$ . The mass of the particle which is not fixed is reset as  $\psi_i h_{\text{tmp}}^2$  with  $m_{i,\text{max}} = 1.05m_i$ , and  $m_{i,\text{min}} = 0.5m_i$  required to determine splitting and merging of particles.

The particles are split and merged according to the  $m_{i,\text{max}}$  and  $m_{i,\text{min}}$  values. The particles are split if the average mass of particle  $\sum_j m_j$  is greater the  $m_{i,\text{max}}$ . The particles are split into 7 daughter particles at a distance  $0.4h$  away from the parent particle in a circle, with one of the particles at the center. The split particles are initially set to have their smoothing lengths as  $h = 0.9h_i$ . In algorithm 2, we describe the splitting procedure in detail. The particle properties are updated in the lines starting with  $\dagger$  as described in section 3.2 to ensure second-order convergence.

In algorithm 3, we show the merging procedure in detail. Two particles are in a neighborhood of each other are merged, if the merged mass  $m_m$  is less than  $m_{i,\text{max}}$  of the particle. The merged particle is placed at the mass-averaged location with the masses of the particles added. The properties

---

**Algorithm 1** Update spacing of particles.

---

- 1: Define  $\Delta s$  for all particles
- 2: **for** all  $i$  of particles which are not fixed **do**
- 3:     find neighbors of  $i$
- 4:     find  $\Delta s_{\min}$ , and  $\Delta s_{\max}$  in the neighborhood
- 5:     find average spacing  $\Delta s_{\text{avg}}$  in the neighborhood
- 6:     **if**  $\frac{\Delta s_{\max}}{\Delta s_{\min}} < (C_r)^3$  **then**
- 7:          $h_{\text{tmp}} \leftarrow \min(\Delta s_{\max}, C_r \Delta s_{\min})$
- 8:     **else**
- 9:          $h_{\text{tmp}} \leftarrow \Delta s_{\text{avg}}$
- 10: **for** all  $i$  of particles which are not fixed **do**
- 11:      $m_i \leftarrow \psi_i h_{\text{tmp}}^2$
- 12:      $m_{i,\max} \leftarrow 1.05m_i$      $m_{i,\min} \leftarrow 0.5m_i$

---

---

**Algorithm 2** Splitting of the particles.

---

- 1:  $\epsilon \leftarrow 0.4$      $\alpha \leftarrow 0.9$
- 2: **for** all  $i$  of particles which are not fixed **do**
- 3:     **if**  $m_i > m_{i,\max}$  **then**
- 4:         split particle  $i$  to 7 daughters
- 5:          $\mathbf{x}_{i,0} \leftarrow \mathbf{x}_i$
- 6:         **for**  $k = 1; k < 7; k++$  **do**
- 7:              $\mathbf{x}_{i,k} \leftarrow \mathbf{x}_i + \epsilon h_i \cos\left(\frac{k\pi}{3}\right)$
- 8:         **for**  $k = 0; k < 7; k++$  **do**
- 9:              $\psi_{i,k} \leftarrow \psi_i$
- 10:              $m_{i,k} \leftarrow \frac{m_i}{7}$ ,     $h_{i,k} \leftarrow \alpha h_i$
- 11:              $\dagger p_{i,k} \leftarrow p_i + (\mathbf{x}_{i,k} - \mathbf{x}_i) \cdot \nabla p_i$
- 12:              $\dagger \mathbf{u}_{i,k} \leftarrow \mathbf{u}_i + (\mathbf{x}_{i,k} - \mathbf{x}_i) \cdot \nabla \mathbf{u}_i$
- 13:              $\dagger \nabla p_{i,k} \leftarrow \nabla p_i$
- 14:              $\dagger \nabla \mathbf{u}_{i,k} \leftarrow \nabla \mathbf{u}_i$

---

after merging are updated as described in section 3.2 to ensure second-order convergence. After merging, the smoothing length is set as [17]

$$h_i = \left( \frac{m_m W(\mathbf{0}, 1)}{m_i W(\mathbf{r}_m - \mathbf{r}_i, h_i) + m_j W(\mathbf{r}_m - \mathbf{r}_j, h_j)} \right)^{1/d}, \quad (\text{A.1})$$

where  $d$  is the number of spatial dimensions.

---

**Algorithm 3** Merging of particles.

---

```

1: for all  $i$  which are not fixed do
2:   find neighbors of  $i$ 
3:   if  $m_i \leq m_{i,\max}$  then
4:     for  $j$  in neighbor indices do
5:        $m_{\text{merge}} \leftarrow m_i + m_j$ 
6:        $m_{\max,\min} \leftarrow \min(m_{i,\max}, m_{j,\max})$ 
7:       if  $m_{\text{merge}} < m_{\max,\min}$  &  $j$  is closest of all neighbors then
8:         store index  $j$  for merging
9: for all  $i$  of particles which are to be merged do
10:  if merge pair of  $i$  is  $j$  and merge pair of  $j$  is  $i$  and  $i < j$  then
11:    update  $\mathbf{x}_i$  using eq. (20)
12:    †update  $\mathbf{u}_i, p_i$  using eq. (22)
13:    †copy gradient properties,  $\nabla \mathbf{u}_i$  and  $\nabla p_i$ 
14:    update  $h_i$  with its merged pair index using eq. (A.1)
15:  else
16:    if merge pairs match and  $i > j$  then
17:      Delete particle  $i$ 

```

---

Algorithm 4 discusses the overall adaptive procedure in detail. In one round of splitting and merging operation, the splitting is performed once and merging is performed thrice to ensure a uniform distribution of mass. After the splitting and merging, particle shifting is performed as discussed in section 3.2 to ensure second-order convergence.

Before the start of the SOC scheme and after every splitting and merging operation, we recompute the particle smoothing length of all the particles using

$$h_i = C \left( \frac{1}{\psi_o} \frac{\sum_j m_j}{N_i} \right)^{1/d}, \quad (\text{A.2})$$

---

**Algorithm 4** Adaptive particle refinement procedure.

---

```
1: while  $t < t_{\text{final}}$  do
2:   for all fluids  $i$  do
3:     †Compute gradients,  $\nabla \mathbf{u}$ , and  $\nabla p$ .
4:     if fluid particles closest to boundary then
5:        $\Delta s_i \leftarrow \Delta s_{\text{min}}$ 
6:     if fluid particles satisfy solution adaptive criteria then
7:        $\Delta s_i \leftarrow \Delta s_{\text{min}}$ 
8:     Update the spacing of particles (algorithm 1)
9:     Split the particles (algorithm 2)
10:    for  $i = 0; i < 3; i++$  do
11:      Merge the particles (algorithm 3)
12:    update the smoothing length using eq. (A.2)
13:    for  $i = 0; i < 3; i++$  do
14:      shift the particles using eq. (18)
15:    †correct the particle properties using eq. (19)
16:    resume the simulation using adaptive SOC scheme (section 3)
```

---

where  $C = 1.2$  is a constant corresponding to the value of smoothing length factor used in the simulation.



## References

1. Monaghan, J.J.. Smoothed Particle Hydrodynamics. *Reports on Progress in Physics* 2005;68:1703–1759.
2. Ramachandran, P., Puri, K.. Entropically damped artificial compressibility for SPH. *Computers and Fluids* 2019;179(30):579–594. doi:10.1016/j.compfluid.2018.11.023.
3. Sun, P., Colagrossi, A., Marrone, S., Antuono, M., Zhang, A.M.. A consistent approach to particle shifting in the  $\delta$  - Plus -SPH model. *Computer Methods in Applied Mechanics and Engineering* 2019;348:912–934. doi:10.1016/j.cma.2019.01.045.
4. Zhang, C., Hu, X.Y.T., Adams, N.A.. A generalized transport-velocity formulation for smoothed particle hydrodynamics. *Journal of Computational Physics* 2017;337:216–232.
5. Adepu, D., Ramachandran, P.. A corrected transport-velocity formulation for fluid and structural mechanics with sph. *Computational Particle Mechanics* 2023;11(1):425–445. URL: <http://dx.doi.org/10.1007/s40571-023-00631-9>. doi:10.1007/s40571-023-00631-9.
6. Vacondio, R., Altomare, C., De Lefte, M., Hu, X., Le Touzé, D., Lind, S., Marongiu, J.C., Marrone, S., Rogers, B.D., Souto-Iglesias, A.. Grand challenges for Smoothed Particle Hydrodynamics numerical schemes. *Computational Particle Mechanics* 2020;URL: <https://doi.org/10.1007/s40571-020-00354-1>. doi:10.1007/s40571-020-00354-1.
7. Negi, P., Ramachandran, P.. Techniques for second order convergent weakly-compressible smoothed particle hydrodynamics schemes without boundaries. *Physics of Fluids* 0;0(ja):null. doi:10.1063/5.0098352.
8. Price, D.J.. Smoothed particle hydrodynamics and magnetohydrodynamics. *Journal of Computational Physics* 2012;231(3):759–794. doi:10.1016/j.jcp.2010.12.011.
9. Hashemi, M.R., Fatehi, R., Manzari, M.T.. A modified SPH method for simulating motion of rigid bodies in Newtonian fluid flows. *International*

- Journal of Non-Linear Mechanics* 2012;47(6):626–638. doi:10.1016/j.ijnonlinmec.2011.10.007.
10. Ravanbakhsh, H., Faghih, A.R., Fatehi, R.. Implementation of improved spatial derivative discretization in DualSPHysics: Simulation and convergence study. *Computational Particle Mechanics* 2023;10(6):1685–1696. doi:10.1007/s40571-023-00582-1.
  11. Negi, P., Ramachandran, P.. How to train your solver: Verification of boundary conditions for smoothed particle hydrodynamics. *Physics of Fluids* 2022;34(11):117125. doi:10.1063/5.0126234.
  12. Negi, P., Ramachandran, P.. How to train your solver: A method of manufactured solutions for weakly compressible smoothed particle hydrodynamics. *Physics of Fluids* 2021;33(12):127108. doi:10.1063/5.0072383.
  13. Bonet, J., Lok, T.S.. Variational and momentum preservation aspects of smooth particle hydrodynamic formulations. *Computer Methods in Applied Mechanics and Engineering* 1999;180(1):97–115. URL: <http://www.sciencedirect.com/science/article/pii/S0045782599000511>. doi:10.1016/S0045-7825(99)00051-1.
  14. Liu, M., Liu, G.. Restoring particle consistency in smoothed particle hydrodynamics. *Applied Numerical Mathematics* 2006;56(1):19–36. doi:10.1016/j.apnum.2005.02.012.
  15. Feldman, J., Bonet, J.. Dynamic refinement and boundary contact forces in SPH with applications in fluid flow problems. *International Journal for Numerical Methods in Engineering* 2007;72(3):295–324. URL: <https://onlinelibrary.wiley.com/doi/abs/10.1002/nme.2010>. doi:10.1002/nme.2010.
  16. Vacondio, R., Rogers, B.D., Stansby, P.K.. Accurate particle splitting for smoothed particle hydrodynamics in shallow water with shock capturing. *International Journal for Numerical Methods in Fluids* 2012;69(8):1377–1410. URL: <https://onlinelibrary.wiley.com/doi/abs/10.1002/flid.2646>. doi:10.1002/flid.2646.
  17. Vacondio, R., Rogers, B., Stansby, P., Mignosa, P., Feldman, J.. Variable resolution for sph: a dynamic particle coalescing and splitting

- scheme. *Computer Methods in Applied Mechanics and Engineering* 2013;256:132–148. doi:10.1016/j.cma.2012.12.014.
18. Barcarolo, D.A., Le Touzé, D., Oger, G., de Vuyst, F.. Adaptive particle refinement and derefinement applied to the smoothed particle hydrodynamics method. *Journal of Computational Physics* 2014;273:640–657. URL: <http://www.sciencedirect.com/science/article/pii/S0021999114004033>. doi:10.1016/j.jcp.2014.05.040.
  19. Chiron, L., Oger, G., de Lefte, M., Le Touzé, D.. Analysis and improvements of Adaptive Particle Refinement (APR) through CPU time, accuracy and robustness considerations. *Journal of Computational Physics* 2018;354:552–575. URL: <http://www.sciencedirect.com/science/article/pii/S0021999117308082>. doi:10.1016/j.jcp.2017.10.041.
  20. Vacondio, R., Rogers, B.D., Stansby, P.K., Mignosa, P., Feldman, J.. Variable resolution for SPH: A dynamic particle coalescing and splitting scheme. *Computer Methods in Applied Mechanics and Engineering* 2013;256:132–148. URL: <http://www.sciencedirect.com/science/article/pii/S0045782512003842>. doi:10.1016/j.cma.2012.12.014.
  21. Vacondio, R., Rogers, B.D., Stansby, P.K., Mignosa, P.. Variable resolution for SPH in three dimensions: Towards optimal splitting and coalescing for dynamic adaptivity. *Computer Methods in Applied Mechanics and Engineering* 2016;300:442–460. URL: <http://www.sciencedirect.com/science/article/pii/S0045782515003813>. doi:10.1016/j.cma.2015.11.021.
  22. Sun, P.N., Colagrossi, A., Marrone, S., Zhang, A.M.. The  $\delta+$ -SPH model: Simple procedures for a further improvement of the SPH scheme. *Computer Methods in Applied Mechanics and Engineering* 2017;315:25–49. URL: <http://www.sciencedirect.com/science/article/pii/S0045782516309112>. doi:10.1016/j.cma.2016.10.028.
  23. Sun, P.N., Colagrossi, A., Marrone, S., Antuono, M., Zhang, A.M.. Multi-resolution Delta-plus-SPH with tensile instability control: Towards high Reynolds number flows. *Computer Physics Communications* 2018;224:63–80. URL: <http://www.sciencedirect.com/science/article/pii/S0010465517303995>. doi:10.1016/j.cpc.2017.11.016.

24. Sun, P.N., Le Touzé, D., Oger, G., Zhang, A.M.. An accurate SPH Volume Adaptive Scheme for modeling strongly-compressible multiphase flows. Part 1: Numerical scheme and validations with basic 1D and 2D benchmarks. *Journal of Computational Physics* 2021;426:109937. doi:10.1016/j.jcp.2020.109937.
25. Ricci, F., Vacondio, R., Tafuni, A.. Multiscale Smoothed Particle Hydrodynamics based on a domain-decomposition strategy. *Computer Methods in Applied Mechanics and Engineering* 2024;418:116500. doi:10.1016/j.cma.2023.116500.
26. Yang, X., Kong, S.C.. Smoothed particle hydrodynamics method for evaporating multiphase flows. *Physical Review E* 2017;96(3):033309. URL: <https://link.aps.org/doi/10.1103/PhysRevE.96.033309>. doi:10.1103/PhysRevE.96.033309.
27. Yang, X., Kong, S.C.. Adaptive resolution for multiphase smoothed particle hydrodynamics. *Computer Physics Communications* 2019;239:112–125. URL: <https://linkinghub.elsevier.com/retrieve/pii/S0010465519300037>. doi:10.1016/j.cpc.2019.01.002.
28. Muta, A., Ramachandran, P.. Efficient and accurate adaptive resolution for weakly-compressible SPH. *Computer Methods in Applied Mechanics and Engineering* 2022;395:115019. doi:10.1016/j.cma.2022.115019.
29. Haftu, A., Muta, A., Ramachandran, P.. Parallel adaptive weakly-compressible SPH for complex moving geometries. *Computer Physics Communications* 2022;277:108377. doi:10.1016/j.cpc.2022.108377.
30. Reyes López, Y., Roose, D., Recarey Morfa, C.. Dynamic particle refinement in SPH: Application to free surface flow and non-cohesive soil simulations. *Computational Mechanics* 2013;51(5):731–741. doi:10.1007/s00466-012-0748-0.
31. Hu, W., Guo, G., Hu, X., Negrut, D., Xu, Z., Pan, W.. A consistent spatially adaptive smoothed particle hydrodynamics method for fluid–structure interactions. *Computer Methods in Applied Mechanics and Engineering* 2019;347:402–424. doi:10.1016/j.cma.2018.10.049.

32. Lind, S., Xu, R., Stansby, P., Rogers, B.. Incompressible smoothed particle hydrodynamics for free-surface flows: A generalised diffusion-based algorithm for stability and validations for impulsive flows and propagating waves. *Journal of Computational Physics* 2012;231(4):1499 – 1523. doi:10.1016/j.jcp.2011.10.027.
33. Ramachandran, P.. automan: A python-based automation framework for numerical computing. *Computing in Science & Engineering* 2018;20(5):81–97. URL: doi.ieeecomputersociety.org/10.1109/MCSE.2018.05329818. doi:10.1109/MCSE.2018.05329818.
34. Gingold, R.A., Monaghan, J.J.. Smoothed particle hydrodynamics: Theory and application to non-spherical stars. *Monthly Notices of the Royal Astronomical Society* 1977;181:375–389.
35. Quinlan, N.J., Basa, M., Lastiwka, M.. Truncation error in mesh-free particle methods. *International Journal for Numerical Methods in Engineering* 2006;66(13):2064–2085. URL: <http://doi.wiley.com/10.1002/nme.1617>. doi:10.1002/nme.1617.
36. Sun, P.N., Le Touzé, D., Oger, G., Zhang, A.M.. An accurate SPH Volume Adaptive Scheme for modeling strongly-compressible multiphase flows. Part 1: Numerical scheme and validations with basic 1D and 2D benchmarks. *Journal of Computational Physics* 2021;426:109937. URL: <https://www.sciencedirect.com/science/article/pii/S0021999120307117>. doi:10.1016/j.jcp.2020.109937.
37. Lüthi, C., Afrasiabi, M., Bambach, M.. An adaptive smoothed particle hydrodynamics (SPH) scheme for efficient melt pool simulations in additive manufacturing. *Computers & Mathematics with Applications* 2023;139:7–27. URL: <https://linkinghub.elsevier.com/retrieve/pii/S0898122123000925>. doi:10.1016/j.camwa.2023.03.003.
38. Pearl, J.M., Raskin, C.D., Michael Owen, J.. FSISPH: An SPH formulation for impacts between dissimilar materials. *Journal of Computational Physics* 2022;469:111533. doi:10.1016/j.jcp.2022.111533.
39. Monaghan, J.J.. Simulating free surface flows with SPH. *Journal of Computational Physics* 1994;110:399–406.

40. Clausen, J.R.. Entropically damped form of artificial compressibility for explicit simulation of incompressible flow. *Physical Review E* 2013;87(1):013309–1–013309–12. URL: <http://link.aps.org/doi/10.1103/PhysRevE.87.013309>. doi:10.1103/PhysRevE.87.013309.
41. Clausen, J.R.. Developing Highly Scalable Fluid Solvers for Enabling Multiphysics Simulation. Tech. Rep. March; Sandia National Laboratories; 2013. URL: <http://prod.sandia.gov/techlib/access-control.cgi/2013/132608.pdf>.
42. Hernquist, L., Katz, N.. TREESPH - A unification of SPH with the hierarchical tree method. *The Astrophysical Journal Supplement Series* 1989;70:419. doi:10.1086/191344.
43. Cleary, P.W., Monaghan, J.J.. Conduction Modelling Using Smoothed Particle Hydrodynamics. *Journal of Computational Physics* 1999;148(1):227–264. doi:10.1006/jcph.1998.6118.
44. Biriukov, S., Price, D.J.. Stable anisotropic heat conduction in smoothed particle hydrodynamics. *Monthly Notices of the Royal Astronomical Society* 2019;483(4):4901–4909. doi:10.1093/mnras/sty3413.
45. Marrone, S., Antuono, M., Colagrossi, A., Colicchio, G., Le Touzé, D., Graziani, G..  $\delta$ -SPH model for simulating violent impact flows. *Computer Methods in Applied Mechanics and Engineering* 2011;200:1526–1542. doi:10.1016/j.cma.2010.12.016.
46. Lastiwka, M., Basa, M., Quinlan, N.J.. Permeable and non-reflecting boundary conditions in SPH. *International Journal for Numerical Methods in Fluids* 2009;61(7):709–724. doi:10.1002/flid.1971.
47. Negi, P., Ramachandran, P., Haftu, A.. An improved non-reflecting outlet boundary condition for weakly-compressible SPH. *Computer Methods in Applied Mechanics and Engineering* 2020;367:113119. doi:10.1016/j.cma.2020.113119.
48. Ramachandran, P.. Development and study of a high-resolution two-dimensional Random Vortex Method. Ph.D. thesis; IIT Madras; Madras; June-2004.

49. Koumoutsakos, P., Leonard, A.. High-resolution simulations of the flow around an impulsively started cylinder using vortex methods. *Journal of Fluid Mechanics* 1995;296:1–38. doi:10.1017/S0022112095002059.